Article

Not peer-reviewed version

The Role Of Sea Breeze In The Coastal Stratocumulus Dissipation Transition In Antofagasta And San Diego

Gabriela Pallauta , Ricardo C. Muñoz , Patricio Arrué , Mónica Zamora Zapata *

Posted Date: 24 February 2025

doi: 10.20944/preprints202502.1779.v1

Keywords: Stratocumulus; Sea breeze; Cloud fragmentation; Cloud dissipation

doi:10.20944/preprints202502.1779.v1

Article

The Role of Sea Breeze in the Coastal Stratocumulus Dissipation Transition in Antofagasta and San Diego

Gabriela Pallauta [1], Ricardo C. Muñoz [2], Patricio Arrué [3] and Mónica Zamora Zapata [1,*]

[1] Departamento de Ingeniería Mecánica, Universidad de Chile
[2] Departamento de Geofísica, Universidad de Chile
[3] Departamento de Ingeniería Mecánica, Universidad Federico Santa María
* Correspondence: mzamora@uchile.cl

Abstract: Coastal Stratocumulus clouds have a diurnal cycle, influenced by solar heating and sea breeze dynamics. These clouds typically thin after sunrise, and some of them fragment and then dissipate, a transition that has proven difficult to predict. In this work, we study the role of sea breeze in the dissipation transition by analyzing observations at two coastal sites, Antofagasta, Chile, and San Diego, CA. Surface measurements of solar irradiance and wind speed allow us to diagnose cloud fragmentation time, dissipation time, and the onset of sea breeze. While both locations differ in meteorological conditions, the transition has a distinctive sequence with similar average times at both locations: sunrise, then sea breeze (43 min later), and finally fragmentation (1.25 h) and dissipation (4.1 h). While the sequence suggests that sea breeze may be causing fragmentation, correlations do not support that hypothesis. Conversely, earlier dissipation events correspond, on average, to weaker wind speeds. Causality between wind speed and solar irradiance was assessed using Convergent Cross Mapping, showing a bidirectional positive correlation. However, the causality is dominated by wind speed, more strongly in Antofagasta than in San Diego, highlighting the role of sea breeze in causing changes in cloudiness.

Keywords: stratocumulus; sea breeze; cloud fragmentation; cloud dissipation

1. Introduction

Present in more than one-fifth of the ocean surface, stratocumulus clouds (Sc) are a type of low-altitude clouds whose convective dynamics result from turbulence that is maintained by a combination of radiative cooling of the upper cloud layer, surface heating, and shear [1]. They have a global impact on the climate due to their high capacity to reflect incoming radiation and emit radiation outward, generating a cooling effect on the global net radiative balance [2]; although their future features are uncertain under climate change conditions [3,4]. The interaction between different processes, such as radiation, turbulence, surface fluxes, sea breeze, and precipitation, controls the physics of Sc [5]. Consequently, the thickness and coverage of Sc are strongly modulated by interactions between synoptic variables, complicating the modeling and understanding of the process [6].

Sc clouds are abundant over cold regions of tropical, subtropical, and mid-latitude oceans because the low ocean temperature produces strong stability in the lower troposphere, promoting their formation [5]. The coasts of Chile and California are part of these locations and where we focus the study. Antofagasta, on the coastal edge of northern Chile, has a desert climate, and the atmospheric boundary layer (ABL) is limited by strong subsidence resulting from the coastal circulation and the dominance of the southeastern sector of the South Pacific High [7]. Between May and November, a higher percentage of cloud ceiling occurrence is observed, reaching nearly 50% in August and September [8]. Similarly, southern California, presents coastal low-altitude stratiform clouds, stratus, and fog, mainly between May and September due to the strong thermal inversion affecting the area during the summer, generated by the North Pacific High, which varies on interannual and interdecadal time scales related to sea surface temperature variability [9].

The diurnal cycle of Sc is strongly influenced by solar radiation along with many other factors [10–12]. During the night, the absence of solar radiation allows the formation of Sc that increases in thickness due to radiative cooling. This growth is countered during the day, as solar heating raises the temperature of the atmospheric boundary layer, causing the cloud base to rise and its thickness to decrease. This thinning can eventually lead to cloud fragmentation and dissipation, especially over coastal regions where the surface fluxes are stronger than over the ocean [13]. The sea breeze is also a consequence of the coastal diurnal cycle. Following the coastal solar heating, warm air rises, creating a divergent motion that invites marine air during the day and reverses overnight. However, marine air can be cooler and moister than over land on some occasions, meaning that the sea breeze advection can mitigate and counteract cloud thinning [14]. This intricate balance could determine if and when the cloud layer dissipates.

The coastal transition of an Sc layer to a fragmented cloud field prior to dissipation has not been extensively studied. There are two observational studies on coastal Sc dissipation stemming from solar irradiance measurements: one proposing methods to detect and characterize the breakup and solar variability [15], and another indicating that inland clouds thin at a characteristic rate prior to dissipation [16]. Some modeling studies have also focused on the evolution of coastal Sc. First, [14] used Large Eddy Simulations (LES) and a Mixed-Layer model (MLM) to describe the diurnal cycle of the ABL over southern California, showing that a later dissipation can occur for conditions of moister land surfaces (lower Bowen ratio), and by activating sea breeze advection. Second, [11] used an MLM to explore the effect of 15 meteorological variables on coastal Sc dissipation time over southern California, finding that initial conditions of thicker clouds and deeper ABLs are related to later dissipation times and also remarking that co-variability strongly impacts the actual effect of each variable. Lastly, [17] modeled a coastal Sc over West Africa using LES; in the case studied, the boundary layer decoupled, forming Cumulus clouds underneath the Sc layer prior to fragmentation. They also reported that top wind shear enhanced entrainment and resulted in a 2-hour earlier fragmentation, while dissipation occurred only 1 hour earlier. None of their diagnostic parameters explained the timing of the fragmentation, and their study was mostly descriptive. Other studies have also linked wind shear to a reduced Sc cloud fraction [18,19], which could potentially contribute to cloud fragmentation. Lastly, a modeling and another observational study continued the analysis of coastal Sc over West Africa, where the first explored the incidence of aerosol concentration on the life cycle of Sc clouds [20], finding that stronger concentrations and smaller particles lead to reduced cloud fraction and earlier dissipation. The second focused on the incidence of initially coupled and decoupled boundary layers on Sc fragmentation [21]. This study identified that there are distinct features for coupled and decoupled transition types, but the cause of the different transitions and the fragmentation drivers were not understood. Therefore, many aspects of the coastal Sc transition remain to be explored.

Convergent Cross Mapping (CCM) is a methodology grounded in nonlinear state space reconstruction, designed to identify causal networks and determine the directionality of interactions between variables. It enables the differentiation between causality and mere correlation within time series data embedded in complex systems, where multiple interacting variables create high-dimensional, dynamic structures [22]. This approach is widely applied across diverse fields, including climatology, epidemiology, and financial regulation, as it facilitates the analysis of complex causal dynamics in systems characterized by nonlinear interactions among multiple factors [23].The ability to detect causality by inferring it from observational data [24], even when masked by noise and where variables may appear uncorrelated, motivated us to apply this approach to examining the interplay between the sea breeze and global horizontal irradiance (GHI) analyzed in this study.

In this paper, we aim to contribute to the understanding of the coastal stratocumulus (Sc) transition by investigating the influence of a critical factor in its development: the sea breeze. Observational data from two locations, Antofagasta and San Diego, are analyzed to characterize the dynamics and temporal evolution of the key moments in the dissipation process and to establish causality within the system. By leveraging observational data, this study incorporates varying daily conditions into the analysis, accounting for natural and complex co-variability effects. Additionally, the comparison between the two locations facilitates the identification of potential differences in the transition process attributable to environmental factors.

The paper is structured as follows: Section 2 details the data and methodologies employed to detect features of clouds and sea breeze. Section 3 presents the results and discussion, beginning with statistical analyses for both locations, followed by correlation analyses, and concluding with an examination of causality. Finally, Section 4 provides the conclusions and discusses potential avenues for future research.

2. Materials and Methods

2.1. Observations in Antofagasta and San Diego

The location of both sites is shown in Figure 1. For Antofagasta, surface observations, ceilometer data, and radiosondes were gathered at the Cerro Moreno airport, (23.4ºS, 70.4ºW, 135 m above sea level), covering 773 days between December 2013 and February 2016. In the case of San Diego, we combine available data from three close sites in La Jolla, covering 252 days between May 2016 and November 2017. The combined data set includes surface data at the EBU 2 building at UC San Diego (32.88°N, 117.23°W), wind speed at the Scripps Pier (32.86°N, 117.25°W)[25], and radiosondes at the NKX Miramar Corps Airport (32.86°N, 117.13°W)[26].

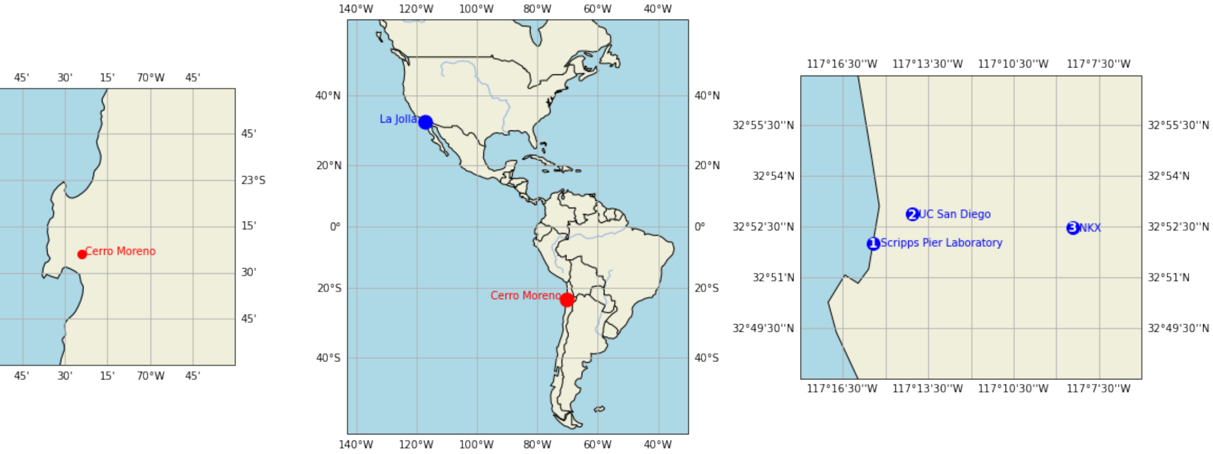

ation of measurements in (a) Antofagasta, where all stations are located at Cerro Moreno; and (b) La Jolla in San Diego, with wind s at point 1, solar measurements at point 2, and other surface measurements and soundings at point 3.

2.1.1. Surface Observations

In Antofagasta and San Diego, surface observations include 5 min resolution time series of surface temperature (T), relative humidity (RH), and downwelling shortwave irradiance or global horizontal irradiance (GHI). For Antofagasta, additional observations of dew point temperature (T_d) and atmospheric pressure (p) were available. Wind speed magnitude (w) and direction (α) had a 5 min time resolution in Antofagasta, while in San Diego, the data at the Pier originally had 1 second resolution, so we averaged them to 5 min whenever necessary. Some days in San Diego also had GHI with 1 second resolution.

These time series are represented by their statistics during the fragmentation and dissipation process. For surface observations, we considered the mean $\bar{x}_{if}$, minimum $x_{min,if}$, maximum $x_{max,if}$, and standard deviation SD_x of temperature, relative humidity, and pressure.

2.1.2. Lower Atmosphere

The state of the lower atmosphere is assessed using radiosondes, with additional ceilometer data in Antofagasta. We considered the morning radiosondes available at 12 UTC at both sites. We process the vertical profiles following a mixed-layer approximation [11], delivering the following variables:

doi:10.20944/preprints202502.1779.v1

number of cloud layers n_{cld}, lifting condensation level z_{LCL}, cloud base height z_b (based on 95% RH), inversion base height z_{ib}, inversion top height z_{it}, ABL mean water mixing ratio q, inversion jump of water mixing ratio Δq, water mixing ratio at 3 km q_{3km}, ABL mean potential temperature θ, inversion jump of potential temperature Δ, potential temperature at 3 km θ_{3km}, ABL mean wind speed w_{ABL}, ABL mean wind direction α_{ABL}, and potential temperature and mixing ratio differences throughout the ABL $\Delta_{dec}\theta$ and $\Delta_{dec}q$–indicators of decoupling [27], as decoupled ABLs could display a larger cloud fraction [28].

In the case of Antofagasta, the ceilometer provided time series of cloud base height, $z_{b,ceil}$, with 1 min resolution. Note that while sounding data is in m above sea level (m a.s.l.), ceilometer data was in m above ground level (m a.g.l.); therefore, data was converted to m a.s.l. for the analysis. Similarly to surface observations, we consider the mean, median, maximum, and standard deviation of cloud base height obtained 1 hour prior to the start of the fragmentation for cloud bases lower than 2500 m. Cloud thickness values are obtained as $h = z_{ib} - z_b$, from radiosonde data, and $h_{ceil} = z_{ib} - z_{b,ceil}$, from radiosonde and ceilometer data.

2.2. Detecting Cloud Fragmentation and Dissipation

We study the cloud fragmentation and dissipation process by analyzing GHI as a proxy for cloudiness, following [15]. The dissipation process consists of three stages. Starting from a cloudy state at sunrise, first, the cloud layer thins uniformly, which translates into a growing GHI progressively reaching the clear sky irradiance. Eventually, the cloud layer transitions from a thin homogeneous layer into a broken cloud field, generating intense GHI variability. Finally, the cloud layer completely dissipates, and the GHI becomes that of a clear sky.

In order to gather statistics for both sites, we first perform a visual inspection of days with a morning cloudy-to-clear transition, resulting in a dataset of 252 days in San Diego and 773 days in Antofagasta. We find the sunrise time t_0 as the first time when the GHI surpasses 5 $\mathrm{W/m^2}$. Then, we detect the times after cloud dissipation using a clear sky detection algorithm [29], where the GHI is compared to a clear sky model irradiance $\mathrm{GHI_{cs}}$, adjusted to observations with the Linke turbidity (LT). With that, we compute the clear sky index k, defined as the ratio between GHI and $\mathrm{GHI_{cs}}$. Then, we find the initial fragmentation time t_i, defined as the first local maximum of GHI with an upper limit of $k < 1.2$. The fragmentation ends when dissipation occurs at t_f, defined as the first time when the clear skies follow for at least 20 min [29]. The thresholds used for the definition of initial and final fragmentation times, the upper limit of 1.2, and the permanence of 20 min were subjected to sensitivity analyses with San Diego data. Varying $k \in (0.6, 1.6)$ led to a constant detection of t_i on 59% of the days starting at $k = 1.2$ (Table A1), while varying the posterior clear time between 10 and 35 min led to a constant detection of 59% below 20 min, with longer times decreasing the days detected (Table A2).

2.3. Detecting the Onset of Sea Breeze

With the wind speed w in m/s and direction α in degrees, we calculated the zonal wind as $u = -w \cdot sin(\alpha)$, the meridional wind as $v = -w \cdot cos(\alpha)$, recovering the wind speed magnitude as $w = \sqrt{|u|^2 + |v|^2}$.

During the morning, the solar heating over coastal land drives the local circulation and strengthens the wind speed. We defined the onset of the sea breeze as the sea breeze start time t_{sb}, defined when there is a sustained increase in wind speed magnitude w for at least 20 min after sunrise. The choice of 20 min was subjected to a sensitivity analysis between 10 and 35 min, where longer times led to a later t_{sb} (Table A3).

We also consider the statistics of sea breeze. First, daily features: daily averages of zonal wind $\overline{u}$, meridional wind $\overline{v}$, wind direction $\overline{\alpha}$, and wind speed magnitude $\overline{w}$; maximum and minimum daily wind speed magnitude, w_{max} and w_{min}; wind speed magnitude at the onset of the sea breeze w_{sb}; and wind speed magnitude at sunrise w_0. Second, fragmentation process features: average, maximum, and minimum wind speed magnitude during cloud fragmentation $\overline{w}_{if}$, $w_{if,max}$, $w_{if,min}$; and the wind speed magnitude at the initial fragmentation time w_i.

Preprints.org (www.preprints.org) | NOT PEER-REVIEWED | Posted: 24 February 2025 doi:10.20944/preprints202502.1779.v1

2.4. Day Selection

After filtering the days that display a cloudy to clear transition in the presence of Sc clouds, only days with existing radiosonde-derived data and a fragmentation process of at least 5 min were considered to observe their distributions and correlations. The resulting case studies in San Diego represent 58% of the total, corresponding to 147 days out of the 252 days studied, and in Antofagasta are 67%, 523 out of 773 days. These locations display a different monthly frequency (Figure 2), and the remaining days correspond to either clear days, days with persisting Sc clouds, or other cloud patterns that did not match the Sc dissipation behavior. While in San Diego these events are less frequent during the fall (October to December) and more frequent during the summer (June to September), in Antofagasta the frequency is more homogeneous throughout the year, with the lowest occurring in February (local summer), and the highest in November (local spring), matching previous results in the literature [8].

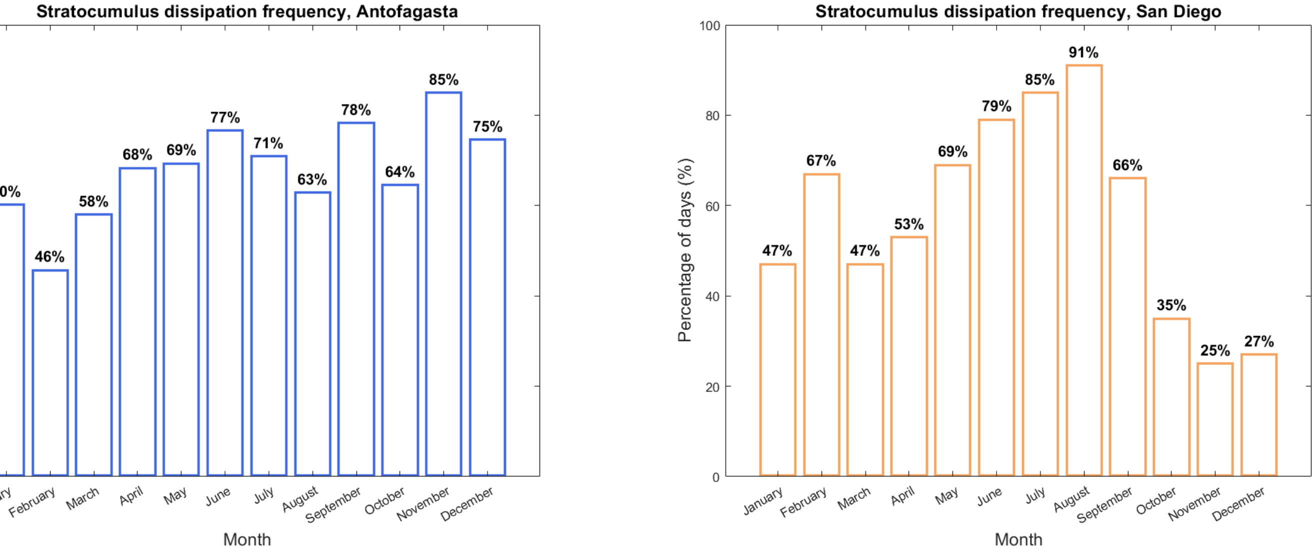

(**a**) (**b**)

Figure 2. Monthly distribution of observed Sc dissipation events in (a) Antofagasta and (b) San Diego.

2.5. Correlation and Causality

We study the relationship among the variables of interest by analyzing inter-correlations and exploring causality using Convergent Cross Mapping (CCM). For correlations, relationships with significant coefficients were analyzed, initially considering a 0.5 correlation threshold which later also included other meaningful but lower correlations to complement the analysis.

CCM is a technique developed for the study of nonlinear complex systems[23], and it allows the identification of causality and determines the direction and sign of the interactions. In this case, we study the relationship between sea breeze and cloudiness by analyzing the time series of wind speed and global horizontal irradiance (GHI). Following [24], we first determine the optimal parameters needed, the time lag τ, using mutual information, and the embedding dimension E. The nonlinearity of the variables was confirmed by examining the decay in prediction accuracy of the Simplex method for forecasting horizons between 1 and 10 units, as in [23], where each unit corresponds to the sampling interval. In order to preserve the original patterns and the different behavior of these two variables over the year, data was not normalized. The analysis focuses on $\tau = 1$ to evaluate direct causality and the relationship between increasing wind speed and cloud dissipation. The embedding dimension E was determined using the *EmbedDimension* function from the pyEDM library [**?**] to adequately capture the underlying system dynamics.

There were some differences in the implementation of CCM for both locations. Since convergence depends on the library size, which is the number of data points in each time series, time resolution matters. Convergence was found to be stable for data series of at least 2500 data points, ensuring good results and minimizing false positives in detecting causal relationships. Therefore, the analysis in Antofagasta covers full 24-hour cycles of consecutive days to capture both diurnal and nocturnal cloud formation and dissipation processes, comprising a single continuous time series to meet convergence conditions since GHI and wind speed series had 5 min resolution. This series was segmented into windows of 8000 data points for evaluation. A total of 785 days, including not only dissipation days, of data recorded at 5-minute intervals were analyzed, with gaps filled by interpolation to avoid discontinuities. The embedding dimension E was systematically evaluated across various library sizes, with $E = 5$ identified as the most stable and representative value.

In the case of San Diego, since wind speed and GHI had a finer original resolution for some days in the dataset, the analysis was conducted on daily time series with 1-minute intervals over 46 days using CCM. The analysis covers the period from April 11 to October 28, 2017, focusing on 10 hours per day (14:00 to 00:00 UTC). The embedding dimension was initially set to $E = 2$ for consistency in temporal dynamics comparisons. Although the GHI-Wind Speed relationship indicated an optimal embedding dimension of $E = 9$, the inverse analysis showed inconsistencies; therefore, $E = 2$ was maintained for robust comparative analysis.

3. Results and Discussion

3.1. Meteorological Conditions and Cloud Properties

The selected days include a wide variety of meteorological conditions, as portrayed in Figure 3, which shows the distributions of the variables obtained from the radiosonde for both locations. A first glimpse reveals that the ABLs that develop Sc dissipation events in San Diego are shallower, moister, and slightly warmer than those in Antofagasta. It is important to note that since both radiosondes are launched at 12:00 UTC, data correspond to an earlier local standard time (LST) for San Diego (04:00 LST) than Antofagasta (08:00 LST). Many of the analyzed Sc events in San Diego corresponded to low inversions, determining low cloud bases. This can not be directly interpreted as San Diego having shallower ABLs in a climatological sense; rather, the Sc that dissipates has a lower inversion at this location, which matches previous observations of persisting Sc displaying a deeper ABL [11].

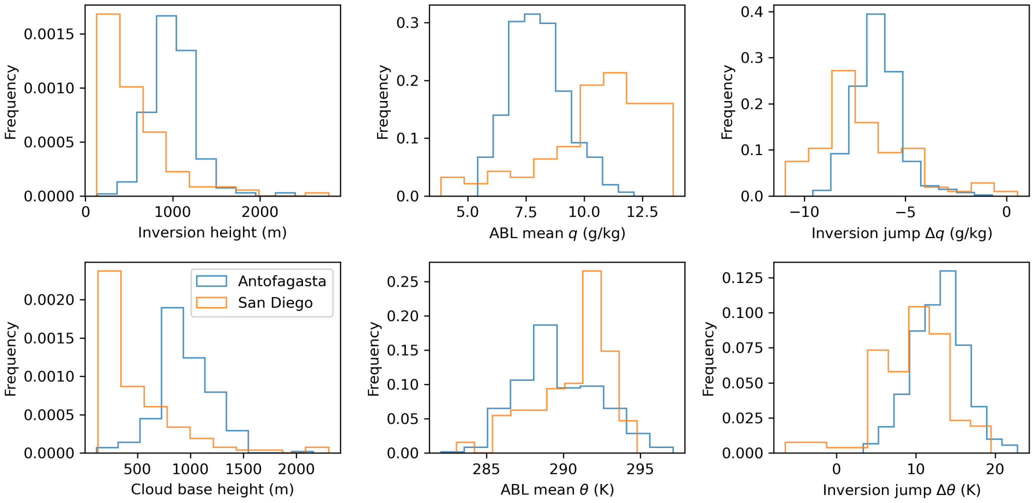

Figure 3. Distributions of the sounding-derived meteorological variables for the dissipation events.

While the radiosonde-derived mean cloud base height was 470 m a.s.l. for all the cases in San Diego, in Antofagasta, this value was 934 m –slightly higher than the ceilometer readings, which reported the following mean values for all the cases an hour prior to fragmentation: a minimum of

830 m, a mean of 866 m, and a maximum of 903 m, a mean difference of 68 m. For the cloud top, represented by the inversion base, the mean height was 523 m in San Diego and 999 m in Antofagasta. This leads to relatively thin layers, with a mean cloud thickness of 117 m in San Diego and 87 m in Antofagasta; however, if considering the ceilometer cloud base, it results in an average of 125 m. This comparison suggests a negative bias of the RH method, meaning that the 95% threshold might be a bit low; however, due to the radiosonde's low resolution with height, it is hard to use a 100% threshold in order to detect cloud layers.

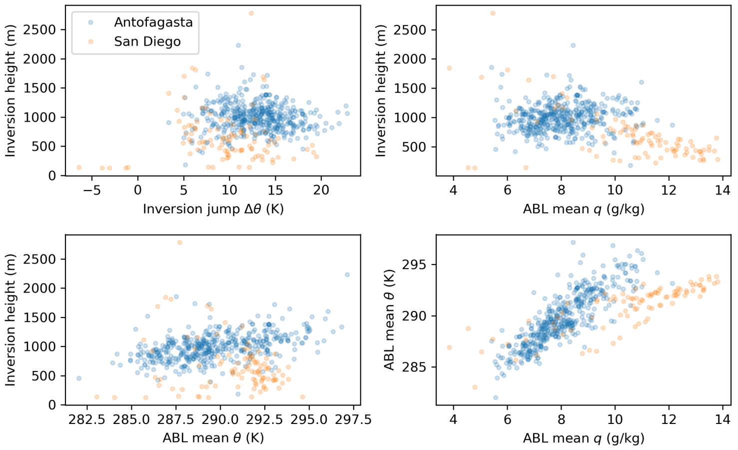

Figure 4. Relationships between the sounding-derived meteorological variables.

Previous studies indicate that the cloud base height of Sc in Antofagasta exhibits a daily cycle characterized by minimum values during the early morning and maximum values during the afternoon, ranging between 600 and 700 m a.s.l, reaching up to 800 meters during the afternoon [30]. According to Figure 3, Sc dissipation events may correspond to relatively high cloud bases for this location. Otherwise, there could be differences stemming from the few measurement points in that height range, forcing the radiosonde algorithm to interpolate the data. Conversely, the inversion base height is consistent with the expected range between 700 and 1200 m [30].

While the range of ABL potential temperature θ is similar for both locations, with a mean difference of 1 K, the ABL total mixing ratio q has a larger mean difference of 2.57 g/kg. A closer look at the joint behavior of some of these variables in Figure 4 reveals that while the inversion strength $\Delta\theta$ does not have a major correlation with the inversion base height z_{ib}, the ABL mean q and θ show a linear relationship –with a different slope at each site. This can be interpreted as a stronger correlation between q and θ for Antofagasta. Another interesting feature is that while inversion height and ABL mean q are anti-correlated for San Diego, which has been interpreted as q being a dependent variable in [11], this is not the case for Antofagasta, where instead z_{ib} shows a correlation with θ.

3.2. Sea Breeze Patterns

To understand the diurnal and annual behavior of the sea breeze, we observe the wind statistics in both sites in Figure 5. While both locations show a diurnal cycle of wind speed magnitude, values are greater in Antofagasta, maxing at 9 m/s, while in San Diego, that limit is near 6 m/s. While in Antofagasta, the meridional wind dominates all throughout the year (Figure 5c), in San Diego, it is the zonal wind (Figure 5d), which weakens in winter. This difference in wind direction is not explained solely by the main coast geography, which is predominantly North-South at both locations and from which we would expect the zonal wind to dominate. The case of Antofagasta differs because the station is located in a peninsula intruding into the southerly coastal winds associated with the South East Pacific Anticyclone. The local sea breeze, the regional circulation, and the terrain west of the station all favor a southerly component of the local near-surface winds.

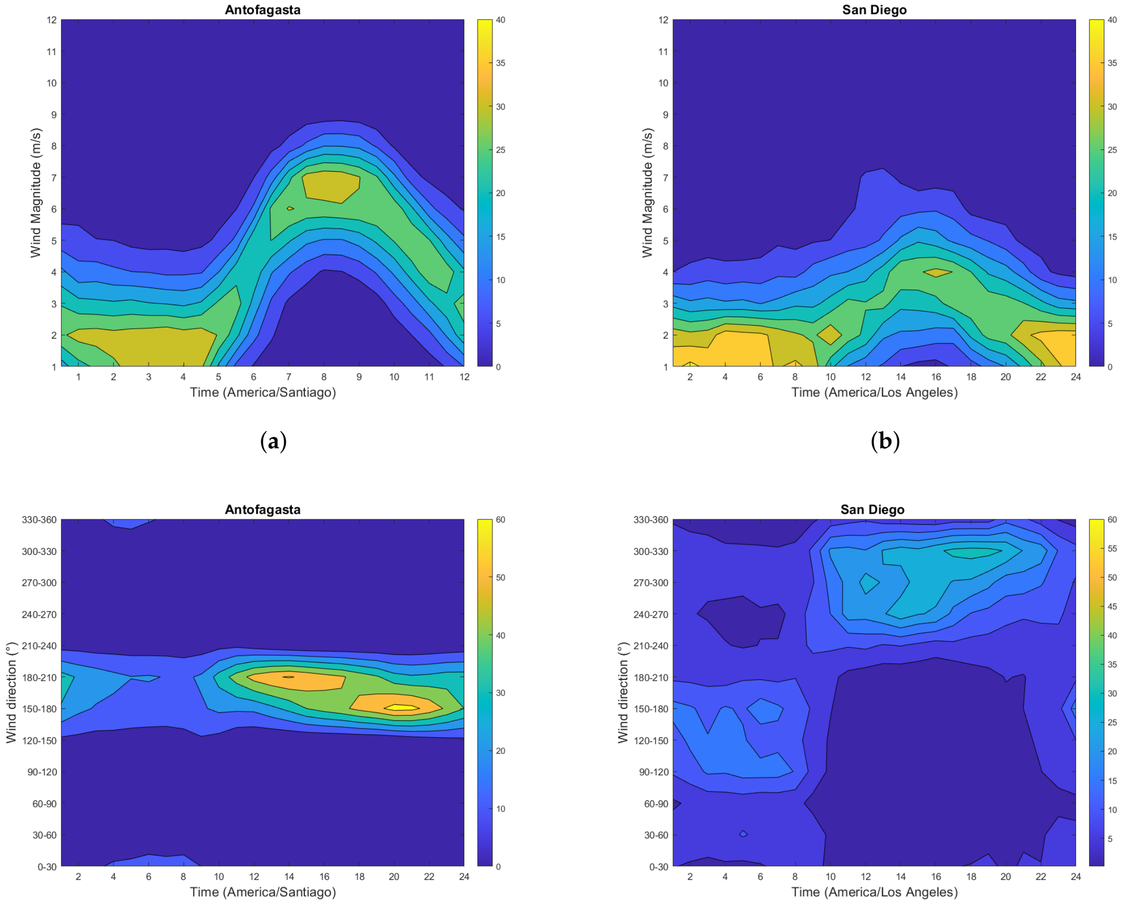

(**a**) (**b**)

(**c**) (**d**)

Figure 5. Average daily profiles of wind speed magnitude in **(a)** Antofagasta and **(b)** San Diego, and wind speed direction in **(c)** Antofagasta and **(d)** San Diego during the studied period. Colors represent the frequency as a percentage.

Considering both magnitude and direction, the diurnal cycle is more defined at Antofagasta, starting near sunrise around 06:00 LST until 20:00 LST, where wind magnitude decays overnight. San Diego presents more variability in the diurnal cycle with weaker wind magnitudes and a wind direction that shifts from a nocturnal zonal wind to a northwestern direction during the day.

3.3. Sample Day Transitions

An example of the fragmentation and dissipation process is illustrated in Figs. 6 and 7, showing GHI, wind speed, and clear sky index for July 26, 2014 in Antofagasta, and July 12, 2016, in San Diego.

Both cases show a strong influence of morning clouds, in Antofagasta (Figure 6), the fragmentation starts around 13:10 UTC and variability persists until 15:50, where clear skies follow 160 min after sunrise. In San Diego, (Figure 7) we can first see GHI attenuation from sunrise, causing a monotonic increase of k until fragmentation starts at 15:15 UTC and ends at 16:35 UTC, 158 min after sunrise.

doi:10.20944/preprints202502.1779.v1

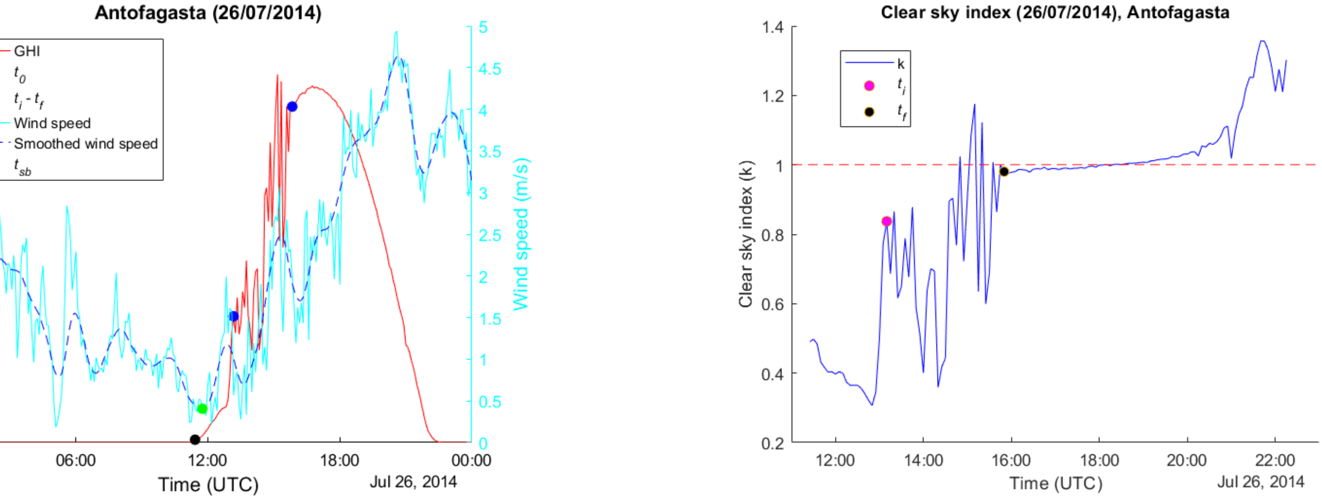

(**a**) (**b**)

Figure 6. Analysis for July 26, 2014 in Antofagasta, showing **(a)** solar irradiance (red), wind speed magnitude (magenta) and its 15-min average (dashed blue), as well as the detected times t_i, t_f and t_{sb}, and (b) the clear sky index for, to display more clearly the detection of the initial and final times of fragmentation, t_i, and t_f.

Fragmentation and dissipation detection are better understood when looking at the clear sky index time series. In Antofagasta, Figure 6b shows that t_i is detected when variability appears, in this case, with a k near 0.8, and dissipation is detected at t_f, after variability ends. For San Diego, Figure 7b shows a shorter fragmentation period, where variability starts at a value of k greater than 1. The detection method works well with both types of curves of k.

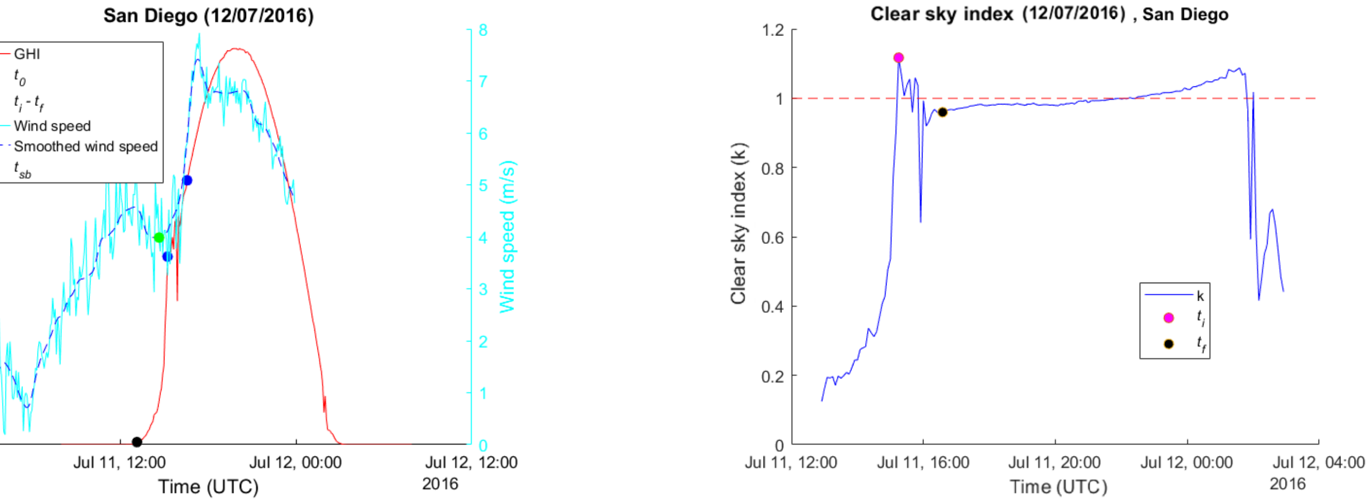

(**a**) (**b**)

Figure 7. Analysis for July 12, 2016 in San Diego, showing **(a)** solar irradiance (red), wind speed magnitude (magenta) and its 15-min average (dashed blue), as well as the detected times t_i, t_f and t_{sb}, and (b) the clear sky index for, to display more clearly the detection of the initial and final times of fragmentation, t_i, and t_f.

We can also observe the dynamics of wind speed in Figure 6a and 7a (magenta and dashed blue). Notably, for these selected days, the wind speed is stronger in San Diego than in Antofagasta, and while the first peaks near noon, the latter does at sunset. In Antofagasta, the daily profile follows the solar diurnal cycle, increasing after sunrise, while in San Diego, there is first a nocturnal increase and then a second growth period after sunrise, which effectively corresponds to the sea breeze and justifies the search only after sunrise.

3.4. The Fragmentation and Dissipation Process

Despite the differences in sea breeze and cloud conditions in both sites, we find that, on average, the fragmentation and dissipation process is strikingly similar. In terms of mean times, as shown in Figure 8, the process at San Diego (Antofagasta) starts at sunrise, 52 min (33 min) later occurs the onset of the sea breeze, followed by the start of the fragmentation at 1.2 h (1.3 h), and ending with dissipation at 3.8 h (4.4 h), followed by clear skies. This transition where we first have sea breeze and then fragmentation occurs not only in the mean sense but also for the majority of the cases: 69% in San Diego and 84% in Antofagasta, and rarely occurs at the exact same time: 4% in San Diego and 3% in Antofagasta.

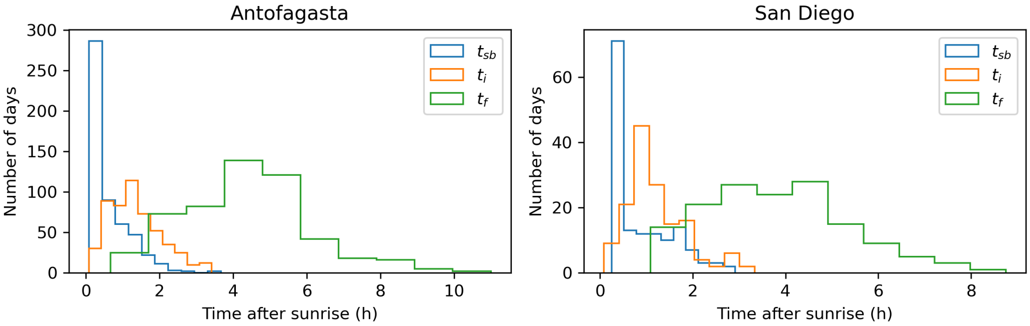

Figure 8. Distribution of variables related to Sc fragmentation, including initial and ending times, t_i and t_f, as well as the onset of sea breeze, t_{sb}.

The whole fragmentation process has a mean duration of 2.6 h in San Diego and 3.1 h in Antofagasta. This distribution is more skewed to the right for San Diego, where 91.3% of the cases last less than 5 h, similar to Antofagasta, where that maximum duration covers 88% of the events. Events with a longer fragmentation process are strongly correlated to a later dissipation, meaning that while the initial time is relatively similar for all cases, the duration of the process does vary, determining the end of the process.

The sea breeze start time is the one with the largest difference (21 min), and its magnitude is slightly stronger in San Diego during fragmentation, with an average of 1.35 m/s at the start and, as expected, increasing to a mean of 2.85 m/s during the process since it occurs at a later time. The same values are 1.1 m/s and 2.01 m/s for Antofagasta.

Many factors can contribute to a later dissipation, but we first focus on our main variable of interest, the sea breeze magnitude during fragmentation, $\overline{w}_{if}$. Comparing the effect of stronger and weaker winds, considered as those greater and lower than the mean, Figure 9 shows that stronger wind is related to a later t_f, confirming the influence of sea breeze on delaying dissipation. Note that the relationship is more robust for Antofagasta due to the greater number of cases considered and that there is considerable overlap between the behavior of weak and strong winds, meaning that other factors can balance sea breeze effects to determine dissipation. Meanwhile, there is no effect of $\overline{w}_{if}$ on t_i, thus resulting in longer fragmentation processes for later dissipation cases.

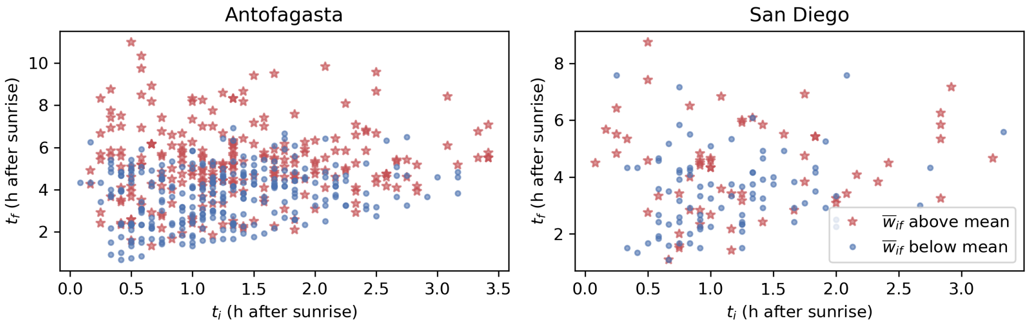

Figure 9. Relationship between fragmentation initial and end times, t_i and t_f, and the average wind speed magnitude during fragmentation, $\overline{w}_{if}$. Cases are separated by strong (red stars) and weak winds (blue dots).

3.5. Relevant Correlations

Figure 10 shows all the relevant correlations within the different variables in each data set. Since we have constructed a large data set, it is hard to assess all relationships in a simple way. In the following, we analyze the most relevant relationships found, first looking at the strongest correlations, greater than 0.5 or smaller than -0.5. Note that correlation indices are reported as ρ_A for Antofagasta and ρ_{SD} for San Diego.

First, it is important to notice that many variables are strongly correlated due to their definitions. For instance, there are many statistics related to wind speed magnitude, temperature, and moisture, and therefore, their positive correlations are not meaningful for our analysis.

Second, we start by focusing on variables related to the fragmentation and dissipation process, mainly t_i and t_f. Initial fragmentation time is correlated to two irradiance statistics at both locations: the mean and minimum solar irradiance during fragmentation $GHI_{min,if}$ ($\rho_A = 0.85$, $\rho_{SD} = 0.77$) and $\overline{GHI}_{if}$ ($\rho_A = 0.57$, $\rho_{SD} = 0.58$). These values indirectly represent cloudiness, and minimum irradiance would correspond to the cloudiest condition, which we can interpret as thicker clouds breaking later. While solar irradiance may indeed be a factor that influences cloud fragmentation, we also know that this value grows with time, which could explain part of the correlation. Modeling efforts could help elucidate this effect.

Other statistics that had slightly weaker correlations are $RH_{max,if}$ ($\rho_A = -0.41$, $\rho_{SD} = -0.2$) and $T_{min,if}$ ($\rho_A = 0.25$, $\rho_{SD} = 0.49$) each stronger at a different location. Combined, they can be interpreted as colder and more saturated surfaces favoring an earlier fragmentation. Another temperature metric appears, $SD_{T,if}$ ($\rho_A = -0.34$, $\rho_{SD} = -0.31$), which is hard to interpret but relates an earlier fragmentation to low thermal variability. Finally, for Antofagasta, we see some effect of cloudiness through $\overline{k}_{if}$ ($\rho_A = 0.26$), which represents that thinner clouds may have a later fragmentation. These results are complex, but at the same time, they hint towards a role marked by solar and thermal surface behavior, suggesting that the sea breeze is not directly causing fragmentation.

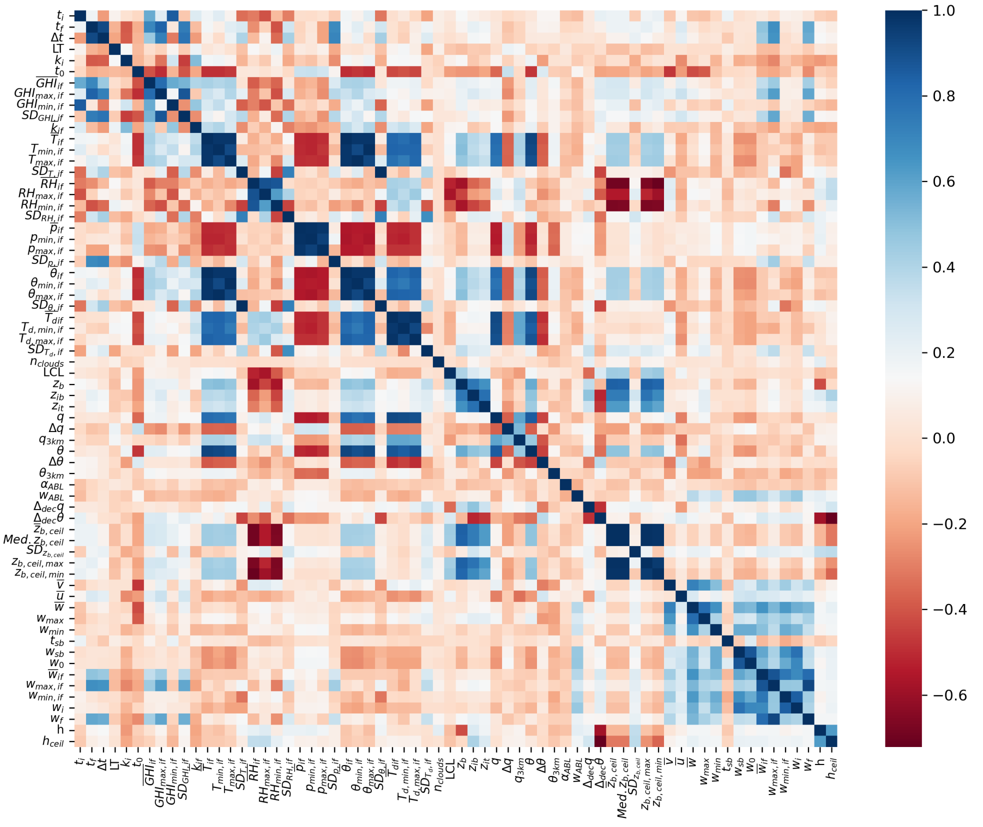

(**a**)

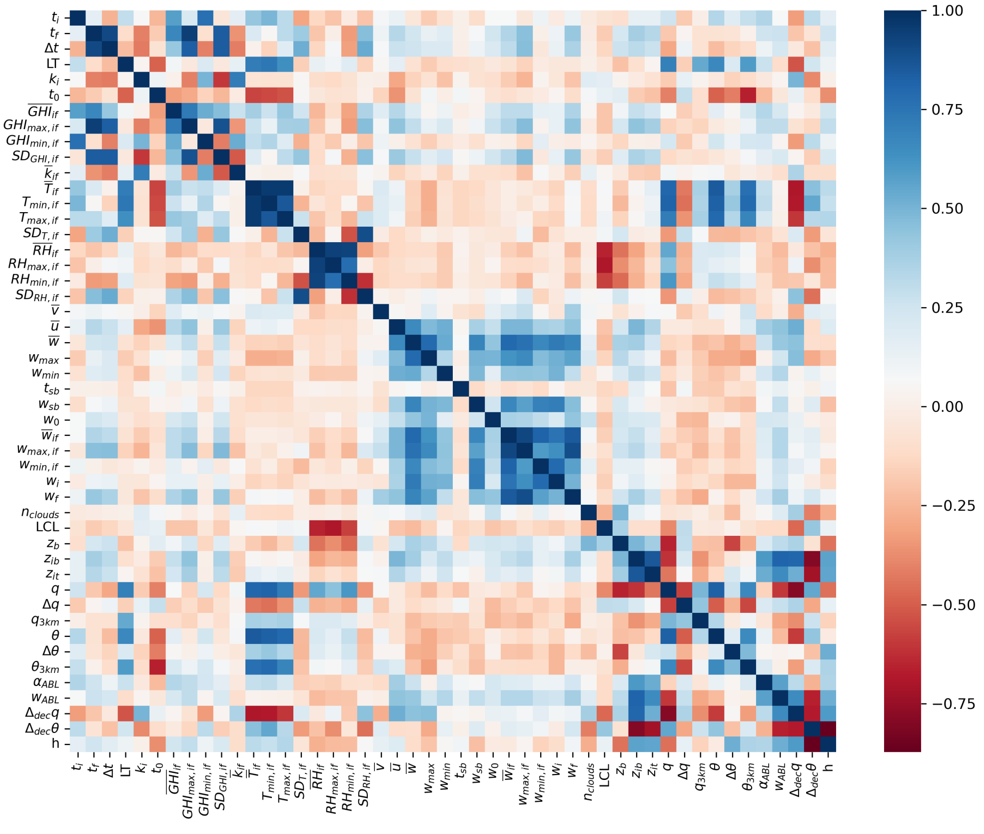

(**b**)

Figure 10. Correlation map for all variables in (**a**) Antofagasta and (**b**) San Diego. Refer to Section 2 or the nomenclature for a description of each index.

Dissipation time, or the end of the fragmentation, t_f, is also correlated to irradiance statistics, as well as to fragmentation duration, at both locations. Only in Antofagasta t_f is correlated to pressure variability and wind statistics. The correlation to fragmentation duration is not relevant, as it was argued when analyzing Figure 9 since Δt is mostly determined by t_f; this is also evident when looking at the correlations with fragmentation duration, being almost identical to those of t_f. The correlated irradiance statistics are the max $GHI_{max,if}$ ($\rho_A = 0.84,\ \rho_{SD} = 0.95$), the mean $\overline{GHI}_{if}$ ($\rho_A = 0.7,\ \rho_{SD} = 0.67$), and the standard deviation $SD_{GHI,if}$ ($\rho_A = 0.74,\ \rho_{SD} = 0.84$). While the mean GHI was also correlated to t_i, now the maximum is related to t_f instead of the minimum, and also the SD, which represents solar variability during fragmentation. Since a longer fragmentation event, related to a later t_f, could display more variability and reach a higher GHI, the correlation is logical. In Antofagasta, the correlation to $SD_{p,if}$ ($\rho_A = 0.69$) can be explained similarly by a longer duration.

The correlations of t_f to wind speed statistics $w_{max,if}$ ($\rho_A = 0.66$) and w_f ($\rho_A = 0.58$) show an incidence of wind speed in cloud dissipation, suggesting that sea breeze effectively delays dissipation in Antofagasta. For San Diego, correlations of t_f to wind statistics were below 0.5, but not for much: maximum wind speed during fragmentation $w_{max,if}$ had $\rho_A = 0.46$, meaning that there is an influence but since dissipation is determined by other factors as well, a weaker influence in San Diego is consistent with the more variable sea breeze behavior. Another statistic that did not surpass the 0.5 mark is the clear sky index at the start of the fragmentation, k_i ($\rho_A = -0.38,\ \rho_{SD} = -0.41$). In this case, k_i is also a proxy for cloudiness, with a lower value representing a thicker cloud. Therefore, we can interpret that initially thicker clouds determine a later dissipation, in agreement with previous studies [11,15].

In terms of meteorological conditions, as mentioned in Section 3.1, the ABL main thermodynamic parameters q and θ are strongly correlated ($\rho_A = 0.85,\ \rho_{SD} = 0.83$), probably corresponding to near saturation conditions since clouds are present in all the considered events. Inversion base height z_{ib} had a strong correlation with w_{ABL} ($\rho_A = 0.7,\ \rho_{SD} = 0.67$), which is the sounding derived wind profile, but not to surface derived wind statistics. This seems counterintuitive but since radiosondes are launched in the early morning, dawn conditions differ from the metrics related to fragmentation. Inversion height z_{ib} is also strongly correlated to q_t in San Diego but not in Antofagasta ($\rho_A = 0.1, \rho_{SD} = -0.61$) as discussed in Section 3.1. In Antofagasta, the inversion height was correlated to decoupling metrics, $\Delta_{dec}\theta$ ($\rho_A = -0.52$) and $\Delta_{dec}q$ ($\rho_A = 0.49$). We usually expect decoupled ABLs to be deeper, as the positive correlation with the moisture decoupling metric, so the negative relation is counterintuitive. When looking at the decoupled states, with the criterion $\Delta_{dec}\theta > 0.5$ K or $\Delta_{dec}q > 0.5$ g/kg [27], we find that there are only 4 days in Antofagasta satisfying the first condition, and none in San Diego. Many other days have negative $\Delta_{dec}\theta$ values as they have a well-mixed temperature profile, and that is what causes the relationship; therefore, this is not a meaningful correlation either. For the moisture decoupling criterion, 51 days in Antofagasta and 20 days in San Diego may be decoupled, which could help sustain the positive correlation.

The radiosonde-derived cloud base height also shows some strong correlations; in Antofagasta, it is to θ ($\rho_A = 0.57$), and in San Diego, to q ($\rho_{SD} = -0.66$), meaning that warmer ABLs in Antofagasta and drier ABLs in San Diego are correlated to a taller cloud base. Both relationships are expected physically, but since the correlated variable differs for each site, once again, it may be a consequence of how they relate to inversion height differently at these two locations. Despite the mentioned differences with ceilometer-derived $z_{b,ceil}$ in Antofagasta, the statistics strongly correlate within a 0.82-0.84 range.

Finally, we analyze cloud thickness, the radiosonde-derived h and the ceilometer-derived h_{ceil} for Antofagasta. Both variables are strongly correlated to $\Delta_{dec}\theta$, for h ($\rho_A = -0.59,\ \rho_{SD} = -0.87$) and for h_{ceil} ($\rho_A = -0.72$). As argued for inversion height, this decoupling metric is not significant as there were not many decoupled days; however, it still is representative of how well-mixed is the temperature profile. In this way, it makes sense that the most well-mixed profiles, represented by a low $\Delta_{dec}\theta_l$, would have thicker clouds due to the effect on saturation, resulting in a sharper liquid water mixing ratio profile. In San Diego, h is also correlated to q_t ($\rho_{SD} = -0.45$), which is a counterintuitive relationship, but it can be explained by its correlation with z_i, as analyzed by [11]. In Antofagasta, the correlation between the two metrics, h and h_{ceil}, is 0.63, which again confirms that the RH method to detect cloud base has room for improvement.

3.6. Causality Between Sea Breeze and Cloudiness

Figure 11 shows the results of the CCM, in particular, the average and standard error of the mean (SME) for the full set of days of each cross-correlation ρ, as a function of the library size, where each unit is equivalent to a sampling frequency of 5 min. The analysis demonstrates that wind speed has a causal influence on global horizontal irradiance (GHI), revealing a positive bidirectional relationship between the two variables. This mutual causation can be conceptualized as a feedback mechanism, where wind speed affects GHI, and GHI, in turn, influences wind speed. Notably, the magnitude of these causal interactions varies between the two study locations while maintaining a consistent positive correlation.

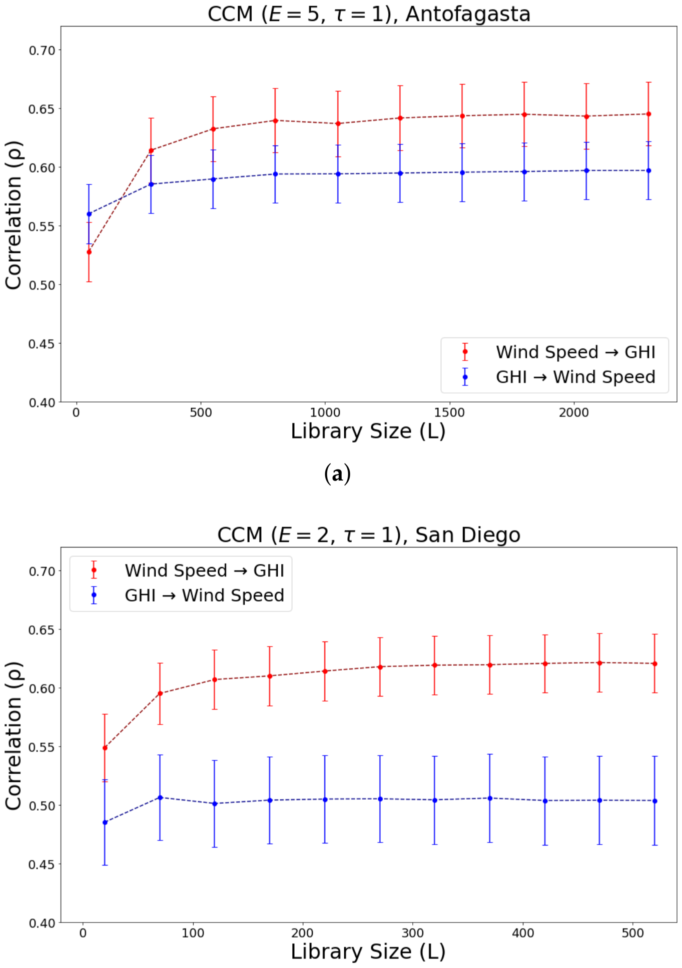

(**a**)

(**b**)

Figure 11. Convergent cross mapping of solar irradiance (GHI) with wind speed magnitude for **(a)** Antofagasta and **(b)** San Diego. The plots include the mean correlation coefficients, and the spread corresponds to the SEM (standard error of the mean).

In San Diego, the causal influence of GHI on wind speed is quantified with the asymptotic correlation ($\rho = 0.51$), while the influence of wind speed on GHI is slightly higher ($\rho = 0.62$). Conversely, in Antofagasta, both causal relationships are notably stronger, with GHI influencing wind speed ($\rho = 0.60$) and wind speed affecting GHI ($\rho = 0.65$). It is also interesting to note that even though the correlations are stronger for Antofagasta, the difference between correlations is larger for San Diego, a sign of stronger bidirectionality and, therefore, a more relevant influence of wind speed

doi:10.20944/preprints202502.1779.v1

over GHI. Comparing these results, we hypothesize that the relatively weaker coefficients in San Diego could be attributed to a diminished temperature gradient between the ocean and the land, influenced by significant urbanization and population density. Such anthropogenic factors may suppress wind subsidence and reduce surface-level wind speeds, thereby weakening the diurnal features of GHI and wind speed. Meanwhile, Antofagasta may have stronger causality due to a more dynamic interplay between wind dynamics and solar irradiance in the region. Antofagasta's geographical and climatic characteristics, defined by its proximity to the Atacama Desert and the Humboldt Current, create pronounced thermal gradients and intensified wind activity. These conditions may strengthen the feedback loop between solar radiation and wind speed, resulting in stronger causation relationships. Regarding the correlation difference being larger in San Diego, this is mainly caused by a reduced influence of GHI on wind speed in this location. This could be related to the less defined sea breeze pattern in San Diego; if the local sea breeze circulation is less frequent or weaker at this location, the causal relationship of GHI could be reduced, while wind speed will always have an advection effect on cloudiness and, therefore, GHI, even if these wind speed changes do not correspond to the sea breeze.

4. Conclusions

We have studied the coastal Stratocumulus fragmentation and dissipation transition in two locations, Antofagasta and San Diego, with a particular emphasis on analyzing the role of sea breeze in this process. Using different observation data, including radiosondes, surface solar, and wind measurements, we were able to extract relevant meteorological variables and detect relevant times. In particular, we used solar irradiance data to detect initial fragmentation time and dissipation time based on variability and clear sky conditions. We also detected the onset time of the sea breeze based on wind measurements.

With a final dataset of 523 days in Antofagasta and 147 days in San Diego presenting Sc dissipation, we observed differences in the Atmospheric Boundary Layer (ABL) state from the morning soundings, finding that these ABLs are shallower, moister, and slightly warmer in San Diego. Despite these differences, cloud fragmentation has a standard sequence: sunrise, then sea breeze, then fragmentation, and finally dissipation, where a clear sky follows. This sequence occurred for 84% of the cases in Antofagasta and 69% in San Diego. Fragmentation and dissipation times are surprisingly similar; for Antofagasta and San Diego, respectively, the sea breeze starts 33 min and 52 min after sunrise, then fragmentation starts at 1.3 h and 1.2 h, ending with dissipation at 4.4 h and 3.8 h.

The transition sequence suggests a causal effect of sea breeze on fragmentation, but correlations were not able to confirm it. The starting fragmentation time was mainly correlated to solar irradiance and thermodynamic variables, dismissing sea breeze as a causing agent. Final fragmentation time, on the other hand, while also correlated to solar irradiance metrics, was correlated to wind speed statistics, suggesting a more direct contribution, although more strongly in Antofagasta than in San Diego. Correlations also informed differences in thermodynamic relationships at the two locations, mainly that the relationship between inversion height and q_t is predominant in San Diego, while in Antofagasta is between inversion height and θ_l.

Finally, we complemented the correlation analysis by studying causation through Convergent Cross Mapping (CCM), exploring the relationship between wind speed magnitude and solar irradiance as a way to understand sea breeze and cloudiness. CCM confirmed a bidirectional causality between the two, with a dominant role of wind speed, suggesting that wind may drive more changes in cloudiness. This dominance was stronger for Antofagasta, which could be due to the differences in local climate and demographics, with conditions in San Diego being more variable than in Antofagasta.

Future research should continue exploring causality with other variables to find robust correlations, such as wind and wind shear at higher altitudes, radar-derived data when available, and cloudiness or solar variability, to focus the data analysis on the fragmentation process. Additionally, research should explore the temporal scales at which these causal relationships can be identified, acknowledging the bidirectional nature of the interactions and the potential for distinct temporal dynamics across system variables. Furthermore, the relationship between sea breeze and stratocumulus cloud cover could be expanded to more regions, accounting for spatial and geographical variability. Modeling efforts using Numerical Weather Prediction or Large Eddy Simulation models could help confirm or elucidate some of these relationships through sensitivity analyses in either idealized or realistic case studies.

Author Contributions: Conceptualization, M.Z.Z.; methodology, G.P., R.C.M, P.A. and M.Z.Z; software, G.P. and M.Z.Z.; formal analysis, G.P., R.C.M, P.A. and M.Z.Z; data curation, G.P. and M.Z.Z; writing—original draft preparation, G.P. and M.Z.Z.; writing—review and editing, R.C.M., P.A and M.Z.Z.; visualization, G.P. and M.Z.Z; supervision, R.C.M. and M.Z.Z.; project administration, M.Z.Z.; funding acquisition, M.Z.Z. All authors have read and agreed to the published version of the manuscript.

Funding: This research was funded by ANID Fondecyt de iniciación grant number 11220918, and Fondecyt Regular grant number 1130111. The APC was funded by ANID Fondecyt de iniciación grant number 11220918.

Institutional Review Board Statement: Not applicable.

Data Availability Statement: Code and processed data are available at https://github.com/mzamora/Sc_wind_Antofagasta_SanDiego. Sounding data [31], surface data at NKX [26], and wind data at the Scripps Pier [25] are public. Other data will be available under request.

Acknowledgments: We thank Jan Kleissl and Cristian Cortés for sharing solar data at UC San Diego. M.Z.Z. thanks Elynn Wu for helpful manuscript suggestions.

Conflicts of Interest: The authors declare no conflicts of interest. The funders had no role in the design of the study, in the collection, analyses, or interpretation of data, in the writing of the manuscript, or in the decision to publish the results.

Abbreviations and symbols

The following abbreviations and symbols are used in this manuscript:

Abbreviations

ABL	Atmospheric Boundary Layer
CCM	Cross Convergent Mapping
LST	Local Standard Time
LT	Linke Turbidity
RH	Relative Humidity
Sc	Stratocumulus

Nomenclature

α	Surface wind speed direction
α_{ABL}	ABL mean wind speed direction from radiosonde data
$\Delta\theta$	Inversion jump of potential temperature
$\Delta_{dec}\theta$	Difference of potential temperature within the ABL, an indicator of decoupling
Δq	Inversion jump of water mixing ratio
$\Delta_{dec}q$	Difference of water mixing ratio within the ABL, an indicator of decoupling
Δt	Duration of the fragmentation process
E	Embedding dimension for CCM
GHI	Global Horizontal Irradiance
GHI_{cs}	Clear sky GHI
h	Cloud thickness estimated with radiosonde data
h_{ceil}	Cloud thickness estimated with ceilometer and radiosonde data
k	Clear sky index
n_{cld}	Number of cloud layers from radiosonde data
ρ	Correlation
p	Atmospheric pressure
q	ABL mean water mixing ratio
q_{3km}	Water mixing ratio at 3 km
SD_x	Standard deviation of variable x during the fragmentation process
T	Temperature
T_d	Dew point temperature
t_0	Sunrise time
t_i	Initial fragmentation time
t_f	Dissipation time
t_{sb}	Initial sea breeze time
τ	Time lag for CCM
θ	ABL mean potential temperature
θ_{3km}	Potential temperature at 3 km
u	Zonal wind
v	Meridional wind
w	Wind speed magnitude
w_{ABL}	ABL mean wind speed magnitude from radiosonde data
$\overline{x}_{if}$	Average of variable x during the fragmentation process
$x_{max,if}$	Maximum of variable x during the fragmentation process
$x_{min,if}$	Minimum of variable x during the fragmentation process
x_0	Value of variable x at sunrise
x_i	Value of variable x when fragmentation starts
x_f	Value of variable x at dissipation
x_{sb}	Value of variable x when sea breeze starts
z_b	Cloud base height estimated from radiosonde data
$z_{b,ceil}$	Cloud base height from the ceilometer
z_{ib}	Inversion base height
z_{it}	Inversion top height
z_{LCL}	Lifting condensation level height

Appendix A

We have included the results of sensitivity tests for the time detection methods. Table A1 shows the effect of maximum k for detecting t_i, Table A2 shows the effect of posterior time for detecting t_f, and Table A3 shows the effect of posterior time on detecting t_{sb}.

Table A1. Sensitivity of initial fragmentation detection (t_i) to the choice of maximum k. The selected value is marked in bold.

Max k	Detected cases	Detection percentage
0.6	98	38%
0.8	122	48%
1.0	140	55%
1.2	**149**	**59%**
1.4	150	59%
1.6	150	59%

Table A2. Sensitivity of dissipation detection (t_f) to the choice of posterior time. The selected value is marked in bold.

Time (min)	Detected cases	Detection percentage
10	149	59%
15	149	59%
20	**149**	**59%**
25	141	56%
30	133	53%
35	130	52%

Table A3. Sensitivity of sea breeze start detection (t_{sb}) and its relation to fragmentation to the choice of posterior time. The selected value is marked in bold.

Time (min)	Cases with $t_{sb} > t_i$	Cases with $t_{sb} = t_i$	Cases with $t_{sb} < t_i$
10	34	5	110
15	39	6	104
20	**44**	**6**	**99**
25	52	6	91
30	57	6	86
35	60	4	85

References

1. Matheou, G.; Teixeira, J. Sensitivity to Physical and Numerical Aspects of Large-Eddy Simulation of Stratocumulus. *Monthly Weather Review* **2019**, *147*, 2621–2639. https://doi.org/10.1175/MWR-D-18-0294.1.
2. Zelinka, M.D.; Randall, D.A.; Webb, M.J.; Klein, S.A. Clearing clouds of uncertainty. *Nature Climate Change* **2017**, *7*, 674–678. https://doi.org/10.1038/nclimate3402.
3. Schneider, T.; Kaul, C.M.; Pressel, K.G. Possible climate transitions from breakup of stratocumulus decks under greenhouse warming. *Nature Geoscience* **2019**, *12*, 163–167. https://doi.org/10.1038/s41561-019-0310-1.
4. Forster, P. The Earth's Energy Budget, Climate Feedbacks and Climate Sensitivity. In *Climate Change 2021 – The Physical Science Basis: Working Group I Contribution to the Sixth Assessment Report of the Intergovernmental Panel on Climate Change*; Intergovernmental Panel on Climate Change (IPCC)., Ed.; Cambridge University Press, 2023; pp. 923–1054. https://doi.org/10.1017/9781009157896.009.
5. Wood, R. Stratocumulus Clouds. *Monthly Weather Review* **2012**, *140*, 2373–2423. https://doi.org/10.1175/MWR-D-11-00121.1.
6. Painemal, D.; Garreaud, R.; Rutllant, J.; Zuidema, P. Southeast Pacific Stratocumulus: High-Frequency Variability and Mesoscale Structures over San Félix Island. *Journal of Applied Meteorology and Climatology* **2010**. Section: Journal of Applied Meteorology and Climatology, https://doi.org/10.1175/2009JAMC2230.1.
7. Rahn, D.A.; Garreaud, R. Marine boundary layer over the subtropical southeast Pacific during VOCALS-REx – Part 1: Mean structure and diurnal cycle. *Atmospheric Chemistry and Physics* **2010**, *10*, 4491–4506. https://doi.org/10.5194/acp-10-4491-2010.

8. Muñoz, R.C.; Zamora, R.A.; Rutllant, J.A. The Coastal Boundary Layer at the Eastern Margin of the Southeast Pacific (23.4°S, 70.4°W): Cloudiness-Conditioned Climatology. *Journal of Climate* **2011**, *24*, 1013–1033. https://doi.org/10.1175/2010JCLI3714.1.
9. Clemesha, R.E.S.; Gershunov, A.; Iacobellis, S.F.; Williams, A.P.; Cayan, D.R. The northward march of summer low cloudiness along the California coast. *Geophysical Research Letters* **2016**, *43*, 1287–1295. https://doi.org/10.1002/2015GL067081.
10. McMichael, L.A.; Mechem, D.B.; Wang, S.; Wang, Q.; Kogan, Y.L.; Teixeira, J. Assessing the mechanisms governing the daytime evolution of marine stratocumulus using large-eddy simulation. *Quarterly Journal of the Royal Meteorological Society* **2019**, *145*, 845–866. https://doi.org/10.1002/qj.3469.
11. Zamora Zapata, M.; Norris, J.R.; Kleissl, J. Coastal Stratocumulus Dissipation Dependence on Initial Conditions and Boundary Forcings in a Mixed-Layer Model. *Journal of the Atmospheric Sciences* **2020**, *77*, 2717–2741. https://doi.org/10.1175/JAS-D-19-0254.1.
12. Schween, J.H.; del Rio, C.; García, J.L.; Osses, P.; Westbrook, S.; Löhnert, U. Life cycle of stratocumulus clouds over 1 year at the coast of the Atacama Desert. *Atmospheric Chemistry and Physics* **2022**, *22*, 12241–12267. https://doi.org/10.5194/acp-22-12241-2022.
13. Ren, Y.; Fu, S.; Xue, H. The sensitivity of a mid-latitude maritime stratocumulus cloud to surface fluxes. *Atmospheric Research* **2023**, *293*, 106912. https://doi.org/10.1016/j.atmosres.2023.106912.
14. Ghonima, M.S.; Heus, T.; Norris, J.R.; Kleissl, J. Factors Controlling Stratocumulus Cloud Lifetime over Coastal Land. *Journal of the Atmospheric Sciences* **2016**, *73*, 2961–2983. https://doi.org/10.1175/JAS-D-15-0228.1.
15. Zamora Zapata, M.; Wu, E.; Kleissl, J. Irradiance Enhancement Events in the Coastal Stratocumulus Dissipation Process. In Proceedings of the Proceedings of the ISES Solar World Congress 2019, Santiago, Chile, 2019; pp. 1–8. https://doi.org/10.18086/swc.2019.42.13.
16. Luccini, E.; Rivas, M. Kinematics and dynamics of the stratocumulus average diurnal dissipation process at Atacama Desert. *Atmospheric Research* **2021**, *255*, 105523. https://doi.org/10.1016/j.atmosres.2021.105523.
17. Pedruzo-Bagazgoitia, X.; de Roode, S.R.; Adler, B.; Babić, K.; Dione, C.; Kalthoff, N.; Lohou, F.; Lothon, M.; Vilà-Guerau de Arellano, J. The diurnal stratocumulus-to-cumulus transition over land in southern West Africa. *Atmospheric Chemistry and Physics* **2020**, *20*, 2735–2754. https://doi.org/10.5194/acp-20-2735-2020.
18. Jeong, J.H.; Witte, M.K.; Smalley, M. Effects of Wind Shear and Aerosol Conditions on the Organization of Precipitating Marine Stratocumulus Clouds. *Journal of Geophysical Research: Atmospheres* **2023**, *128*, e2023JD039081. https://doi.org/10.1029/2023JD039081.
19. Zamora Zapata, M.; Heus, T.; Kleissl, J. Effects of Surface and Top Wind Shear on the Spatial Organization of Marine Stratocumulus-Topped Boundary Layers. *Journal of Geophysical Research: Atmospheres* **2021**, *126*, e2020JD034162. https://doi.org/10.1029/2020JD034162.
20. Delbeke, L.; Wang, C.; Tulet, P.; Denjean, C.; Zouzoua, M.; Maury, N.; Deroubaix, A. The impact of aerosols on stratiform clouds over southern West Africa: a large-eddy-simulation study. *Atmospheric Chemistry and Physics* **2023**, *23*, 13329–13354. https://doi.org/10.5194/acp-23-13329-2023.
21. Zouzoua, M.; Lohou, F.; Assamoi, P.; Lothon, M.; Yoboue, V.; Dione, C.; Kalthoff, N.; Adler, B.; Babić, K.; Pedruzo-Bagazgoitia, X.; et al. Breakup of nocturnal low-level stratiform clouds during the southern West African monsoon season. *Atmospheric Chemistry and Physics* **2021**, *21*, 2027–2051. https://doi.org/10.5194/acp-21-2027-2021.
22. Tsonis, A. Convergent Cross Mapping: Theory and an Example. In *Advances in Nonlinear Geosciences*; Springer, Cham, 2017; p. 587– 600. https://doi.org/10.1007/978-3-319-58895-7_27.
23. Sugihara, G.; May, R.; Ye, H.; Hsieh, C.h.; Deyle, E.; Fogarty, M.; Munch, S. Detecting Causality in Complex Ecosystems. *Science* **2012**, *338*, 496–500. https://doi.org/10.1126/science.1227079.
24. Rybarczyk, Y.; Zalakeviciute, R.; Ortiz-Prado, E. Causal effect of air pollution and meteorology on the COVID-19 pandemic: A convergent cross mapping approach. *Heliyon* **2024**, *10*. https://doi.org/10.1016/j.heliyon.2024.e25134.
25. Coastal Data Information Program (CDIP). Station 73 - SCRIPPS PIER, LA JOLLA CA.
26. Iowa State University. IEM :: Download ASOS/AWOS/METAR Data.
27. Jones, C.R.; Bretherton, C.S.; Leon, D. Coupled vs. decoupled boundary layers in VOCALS-REx. *Atmospheric Chemistry and Physics* **2011**, *11*, 7143–7153. https://doi.org/10.5194/acp-11-7143-2011.
28. Goren, T.; Rosenfeld, D.; Sourdeval, O.; Quaas, J. Satellite Observations of Precipitating Marine Stratocumulus Show Greater Cloud Fraction for Decoupled Clouds in Comparison to Coupled Clouds. *Geophysical Research Letters* **2018**, *45*, 5126–5134. https://doi.org/10.1029/2018GL078122.

29. Reno, M.J.; Hansen, C.W. Identification of periods of clear sky irradiance in time series of GHI measurements. *Renewable Energy* **2016**, *90*, 520–531. https://doi.org/10.1016/j.renene.2015.12.031.
30. Zamora Aguirre, R. Caracterización Observacional de la Capa Límite Marina en Antofagasta. Master's thesis, Universidad de Chile, 2010.
31. University of Wyoming. Atmospheric Soundings.